Original Article

Monoenergetic reconstructions and iodine density maps for visualization of coronary artery stents using 8-cm dual-layer detector spectral computed tomography: an *in vitro* phantom study

Lihong Chen[1#], Ning Pan[2#], Bin Hu[1], Yaofeng Li[3], Shushan Dong[4], Yinan Zhou[4], Jianxin Guo[1], Jian Yang[1], Yongbai Luo[5], Zhijie Jian[1]

[1]Department of Radiology, The First Affiliated Hospital of Xi'an Jiaotong University, Xi'an, China; [2]Bayer Healthcare Company Limited, Xi'an, China; [3]Department of Radiology, the East District of The First Affiliated Hospital of Xi'an Jiaotong University, Xi'an, China; [4]Philips HealthCare, Clinical Science, Beijing, China; [5]Department of Cardiovascular Medicine, The First Affiliated Hospital of Xi'an Jiaotong University, Xi'an, China

Contributions: (I) Conception and design: L Chen, N Pan; (II) Administrative support: Y Luo, Z Jian, J Guo, J Yang; (III) Provision of study materials or patients: Y Luo, B Hu, Y Li; (IV) Collection and assembly of data: L Chen, S Dong, Y Zhou; (V) Data analysis and interpretation: L Chen, N Pan, Z Jian; (VI) Manuscript writing: All authors; (VII) Final approval of manuscript: All authors.

[#]These authors contributed equally to this work.

Correspondence to: Zhijie Jian, MD. Department of Radiology, The First Affiliated Hospital of Xi'an Jiaotong University, 277 West Yanta Road, Yanta District, Xi'an 710061, China. Email: Jianzhijie@xjtufh.edu.cn; Yongbai Luo, MD. Department of Cardiovascular Medicine, The First Affiliated Hospital of Xi'an Jiaotong University, 277 West Yanta Road, Yanta District, Xi'an 710061, China. Email: dr.luoy@qq.com.

Background: The effectiveness of coronary computed tomography (CT) angiography in assessing stent restenosis is hindered by heavy metal artifacts. This study aimed to evaluate the image quality of monoenergetic reconstructions and iodine density map for coronary stent imaging using an 8-cm dual-layer detector spectral CT.

Methods: In this study, 8 stents with a diameter <3 mm (group A) and 10 with a diameter ≥3 mm (group B) were placed in plastic tubes filled with iodinated contrast media and scanned. The internal diameter of the prepared stents was then measured by intravascular ultrasound. The reconstructed images included iodine density maps, conventional images, and different energy levels. The visualization of the stent lumen and stent structure was subjectively assessed using a 4-point Likert scale. The objective evaluation was performed using the in-stent lumen signal-to-noise ratio (SNRis), non-stent lumen SNR (SNRns), internal diameter difference (IDD), and blooming artifact index (BAI). The Friedman test and analysis of variance were used for multiple comparisons.

Results: For lumen visualization, the optimal monoenergetic images received the highest score for both group A (2.56±0.51) and group B (3.1±0.55). Multiple comparisons showed that there were significant differences between the optimal monoenergetic images and iodine density maps. However, for stent structure, iodine density maps received the highest score for group A (3.0±0.52) and group B (3.8±0.41). For quantitative assessment, the optimal monoenergetic images had the highest SNRis and SNRns, while the iodine density maps had the lowest SNRis and SNRns. For IDD and BAI, the iodine density maps yielded the smallest value.

Conclusions: The monoenergetic images on the second-generation dual-layer detector CT provide better visualization of the lumen and higher SNR. However, iodine density maps are superior for evaluating stent structure and IDD and BAI compared to monoenergetic and conventional reconstructions.

Keywords: Computed tomography (CT); coronary artery disease; in-stent restenosis; stent; dual-layer detector

Submitted Apr 17, 2024. Accepted for publication Aug 15, 2024. Published online Sep 24, 2024.
doi: 10.21037/qims-24-786
View this article at: https://dx.doi.org/10.21037/qims-24-786

Introduction

Coronary artery disease remains a leading cause of noncancer-related death. One of the commonly used therapeutic procedures for treating acute coronary syndromes is coronary stenting (1,2). Despite the significant progress in stent manufacturing, including thinner structures and longer drug-eluting periods, in-stent restenosis still occurs in about 5% of stenting cases (3,4). However, the effectiveness of coronary computed tomography (CT) angiography (CCTA) in assessing postprocedural in-stent restenosis is limited due to heavy metal artifacts (5,6). It has been reported that 13% of the stents in conventional CCTA images are unassessable (6), and the rate of false positives or inconclusive findings is 25% among the assessable stents (7).

Several reports have discussed the use of dual-energy technology to reduce metal artifacts and improve the visualization of the in-stent lumen in CCTA (8-10). This technique involves separating the X-ray into high- and low-energy portions during the dual-energy CT scan. This allows for the reconstruction of virtual monoenergetic and other functional images, such as iodine density maps (11). The higher-energy X-ray results in fewer metal artifacts in high-energy monoenergetic images and better visualization of the lumen in stented coronary arteries. The iodine density maps provide information on the equivalent iodine concentration of each pixel (12). Previous studies have shown that the iodine density maps enhance lesion visualization compared to conventional CT images (13,14). However, its contribution to the assessment of in-stent restenosis has not been investigated.

In contrast to tube-based dual-energy scanning, which uses different emitted energy spectra, the detector-based solution uses a single X-ray source and a special dual-layer structure to separate the low-energy and high-energy parts of the X-rays. The upper layer measures the low-energy portion of the emitted spectrum, while the lower layer detects and measures the high-energy photons (15). This approach allows for dual-energy postprocessing in the raw data space, reducing metal artifacts and improving image quality. By combining the high- and low-energy data, conventional images equivalent to those from a single-energy scanner can be reconstructed. From the basic pair raw data, the photoelectric and Compton scatter basis images can be generated, from which additional material composition images and virtual monoenergetic images can be reconstructed (16). In 2021, a second-generation dual-layer detector CT with a wider (8 cm) detector became commercially available. This enhancement in temporal resolution makes it more suitable for CCTA and improves the visualization of the in-stent lumen and stent structure.

The objective of this study was to compare the additional value of monoenergetic images and iodine density maps in visualizing the in-stent lumen and the stent structure on the 8-cm dual-layer detector spectral CT with conventional reconstructions.

Methods

Experimental setup

As described in previous studies (17), plastic tubes with internal diameters ranging from 2.5 to 4.5 mm were used to simulate coronary arteries. A total of 18 stents, made of different materials and structures, were employed in this experiment. A cutoff value of 3 mm is recommended in the 2010 multisocietal appropriate use criteria to predict the certainty of the outcome of coronary stenting (18). Therefore, we divided the stents into two groups: 8 stents had diameters less than 3 mm (group A) and 10 had diameters equal to or greater than 3 mm (group B) (*Table 1*). These stents were carefully placed into the polyvinyl chloride plastic tubes through balloon dilatation by a cardiac interventionalist. To prevent any movement during the experiment, all stents were positioned as close to the tube wall as possible. Iodinated contrast media (350 mg/L; iohexol; Omnipaque, GE HealthCare, Chicago, IL, USA) and saline were mixed to achieve an iodine concentration of 11 mg/L (dilution ratio of 1:30.8) and injected into the plastic tubes. Any air bubbles adhering to the tube wall and stents were removed by flicking. Intravascular ultrasound (IVUS) was used to accurately measure the internal diameter of the prepared stents. The ends of the plastic tubes were securely tied to prevent any leakage of the contrast media. These prepared tubes were then arranged in two layers on a customized tray

Table 1 Characteristics of the examined stents

Stent number	Nominal external diameter (mm)	Internal diameter (mm)	Length (mm)	Struct thickness (mm)	Company	Material	Coating
1	2.25	2.01	8	0.081	Boston Scientific	Platinum-chromium alloy	Everolimus
2	4	3.59	38	0.081	Boston Scientific	Platinum-chromium alloy	Everolimus
3	2.25	1.73	38	0.074	Boston Scientific	Platinum-chromium alloy	Everolimus
4	3.5	2.43	38	0.081	Boston Scientific	Platinum-chromium alloy	Everolimus
5	2.5	2.21	38	0.081	Boston Scientific	Platinum-chromium alloy	Everolimus
6	3	2.78	8	0.074	Boston Scientific	Platinum-chromium alloy	Everolimus
7	2.5	2.24	29	0.084	Jiwei Medical	Cobalt-chromium alloy	Rapamycin
8	2.25	2.00	14	0.084	Jiwei Medical	Cobalt-chromium alloy	Rapamycin
9	4	3.89	29	0.084	Jiwei Medical	Cobalt-chromium alloy	Rapamycin
10	3	2.93	14	0.084	Jiwei Medical	Cobalt-chromium alloy	Rapamycin
11	2.5	2.26	13	0.086	Mircoport	Cobalt-chromium alloy	Rapamycin
12	4	3.74	13	0.086	Mircoport	Cobalt-chromium alloy	Rapamycin
13	2.25	2.10	13	0.086	Mircoport	Cobalt-chromium alloy	Rapamycin
14	3.5	2.97	13	0.086	Mircoport	Cobalt-chromium alloy	Rapamycin
15	3	2.79	13	0.086	Mircoport	Cobalt-chromium alloy	Rapamycin
16	2.75	2.23	13	0.086	Mircoport	Cobalt-chromium alloy	Rapamycin
17	3.5	3.42	29	0.084	Mircoport	Cobalt-chromium alloy	Rapamycin
18	3	2.79	24	0.084	Mircoport	Cobalt-chromium alloy	Rapamycin

with approximately 1 cm between the stents and placed in a square acrylic container, parallel to the Z-axis of the CT scanner (*Figure 1*). Finally, the container was filled with homogenized vegetable oil (Yihai Kerry Aravana Holdings Co., Shanghai, China) to mimic epicardial adipose tissue and positioned at the isocenter of the gantry. *Figure 1* provides an illustration of the setup used for the experiment.

CT data acquisition

CT data were acquired using a second-generation dual-layer detector spectral CT scanner (CT 7500, Philips Healthcare, Amsterdam, The Netherlands) with a simulated electrocardiogram (ECG) signal at a heart rate of 60 beats per minute for prospective ECG-triggered acquisition. The scanning parameters, which were similar to those of routine clinical scans with specific optimization in dose modulation, were as follows: tube voltage, 120 kVp; tube current, 125 mAs; slice collimation, 128×0.625 mm, and rotation time, 0.27 seconds. The exposure was set at the window of 75% R-R interval of the ECG. The reconstruction parameters were set as follows: field of view, 250 mm × 250 mm; matrix, 512×512; slice thickness, 0.67 mm; increment, 0.35 mm; and statistical iterative reconstruction, iDose4 at level 3. High-resolution convolution kernel (CD) was used, as it provides better stent visualization (19). The reconstructed images included iodine density maps, conventional images, and monoenergetic images at 17 different energy levels ranging from 40 to 200 keV in increments of 10 keV.

CT data analysis

All reconstructed images were transferred to the scanner's standard workstation (IntelliSpace Portal version 12.1, Philips Healthcare). Prior to subjective and quantitative assessments, multiplanar reformats displaying the longitudinal stent lumen were reconstructed. According to previous studies, a higher window center level reduces streak-like artifacts in the images, and the window width is usually set to about 2.5 times that of the window center (20). Thus,

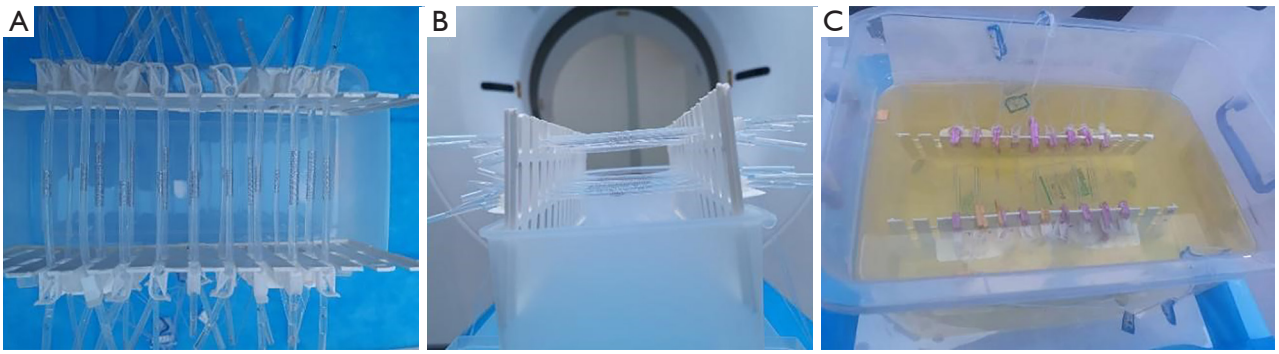

Figure 1 Photographs of the phantom setup. (A,B) The vertical and front views of the prepared tubes arranged in two layers on a customized tray. (C) A container filled with homogenized vegetable oil to mimic epicardial adipose tissue.

a fixed window width of 4,000 Hounsfield units (HU) and a window center of 1,500 (HU) were used during assessments.

For subjective evaluation, a double-blind assessment of the lumen and structure of the stents was conducted by two cardiothoracic radiologists with more than 8 years of experience using a Likert 4-point scale. The scoring scheme for the image quality of the stent lumen was as follows: 4 points for excellent quality with few or no artifacts in the stent lumen, 3 points for good quality with some artifacts present but not affecting diagnostic confidence, 2 points for moderate quality with artifacts that to some extent deteriorate diagnostic confidence, and 1 point for poor quality with a poor display of the stent lumen. Meanwhile, the scoring scheme for stent structure was as follows: 4 points for excellent stent structure display with clear definition, 3 points for good quality with slightly blurred scaffold borders that do not obscure the display of structure, 2 points for moderate quality with blooming artifacts that affect the display of stent structure and reduce diagnostic confidence, and 1 point for poor quality with significant blooming artifacts that completely obscure the stent structure.

The quantitative evaluation consisted of geometric parameters and signal-to-noise ratio (SNR). To obtain the average visible internal and external diameter of each stent, three straight-line regions of interest (ROIs) were drawn at the proximal, middle, and distal points, as illustrated in *Figure 2*. The geometric parameters, including blooming artifact index (BAI) and internal diameter difference (IDD), were subsequently calculated according to the following formula:

BAI = $(ED_{CT} - ID_{CT})/ED_{CT} \times 100\%$, where the ED_{CT} and ID_{CT} are the external diameter and internal diameter measured on CT imaging, respectively.

IDD = $(ID_{IVUS} - ID_{CT})/ID_{IVUS} \times 100\%$, where ID_{IVUS} is the internal diameter measured on IVUS, and ID_{CT} is the internal diameter measured on CT imaging.

In addition to the geometric parameters mentioned above, the SNR was also analyzed by the following steps: three elliptical ROIs were placed at the proximal, middle, and distal points of the stent lumen, with care taken to avoid stent structures and blooming artifacts and maximize the ROI size. Two elliptical ROIs copied from the previous step were then placed outside both ends of the stent, as illustrated in *Figure 2B*. Finally, the average attenuation and standard deviation (SD) (representing noise) were generated for the in-stent and non-stent ROIs, respectively. The SNR of the in-stent and non-stent lumen was calculated using the following formula:

SNR_{is} or SNR_{ns} = average attenuation/standard deviation, where SNR_{is} and SNR_{ns} are the SNR of the in-stent and non-stent lumen, respectively.

IVUS data acquisition and evaluation

All IVUS imaging were performed using a 40-MHz IVUS catheter (OptiCross, Boston Scientific Corporation, Natick, MA, USA). The IVUS catheter was placed distal to the stents and then pulled back with a motorized pullback system at 0.5 cm/s. During pullback, grayscale IVUS was recorded. IVUS measured the internal diameter of the distal and proximal end of the stent, as well as the middle of the stent, which was consistent with the CT diameter measurement (*Figure 3*). IVUS images were analyzed by an experienced interventional cardiologist.

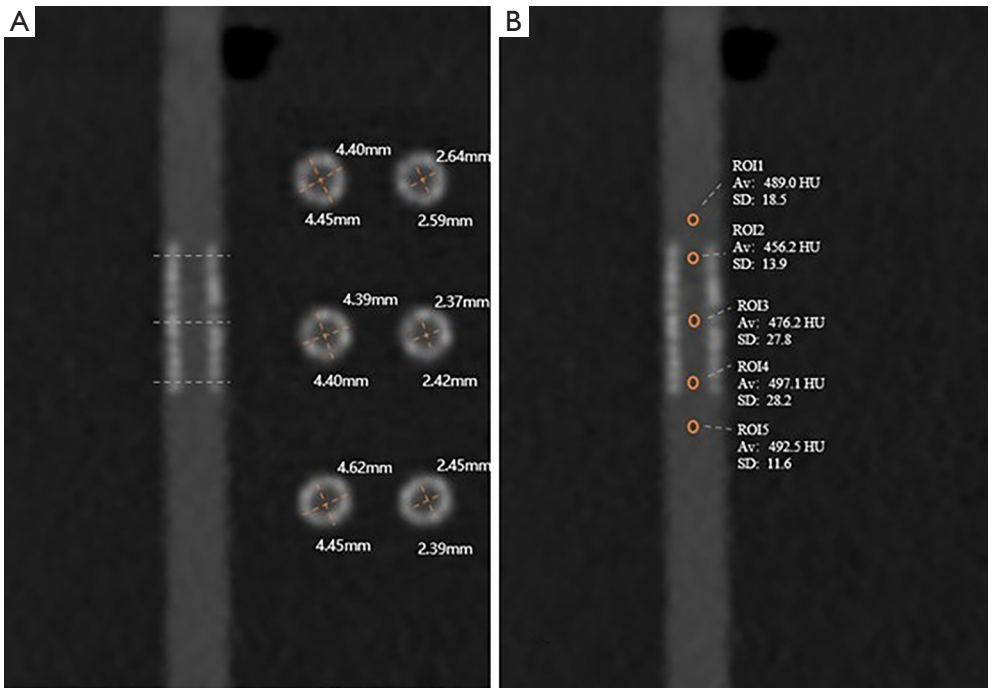

Figure 2 ROIs for the quantitative evaluations. (A) A representation of the internal and external diameter measurements of the stent (number 12). (B) ROIs were placed for the measurement of mean attenuation and standard deviation of the in-stent and non-stent lumens. ROI, region of interest; Av, average; HU, Hounsfield unit; SD, standard deviation.

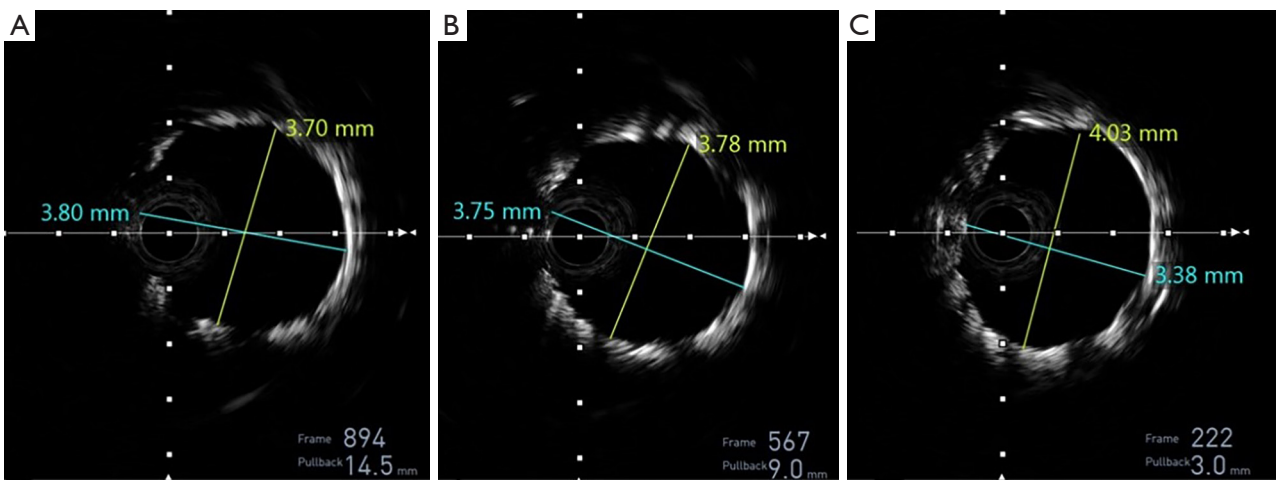

Figure 3 IVUS measurements of the inner diameter of the stent (number 12). IVUS, intravascular ultrasound.

Statistical analysis

GraphPad Prism 9.0 software (GraphPad Software, Inc., La Jolla, CA, USA) was used for statistical analysis. Enumerated data are expressed as frequencies. The Kolmogorov-Smirnov test was used to determine the normal distribution of continuous data. Normally distributed data are expressed as the mean ± SD, and nonnormally distributed data are expressed as the median and upper and lower quartiles. Linear weighted Kappa coefficient was used to assess the interrater agreement of subjective evaluations conducted by two radiologists. Paired ordinal scores of the optimal

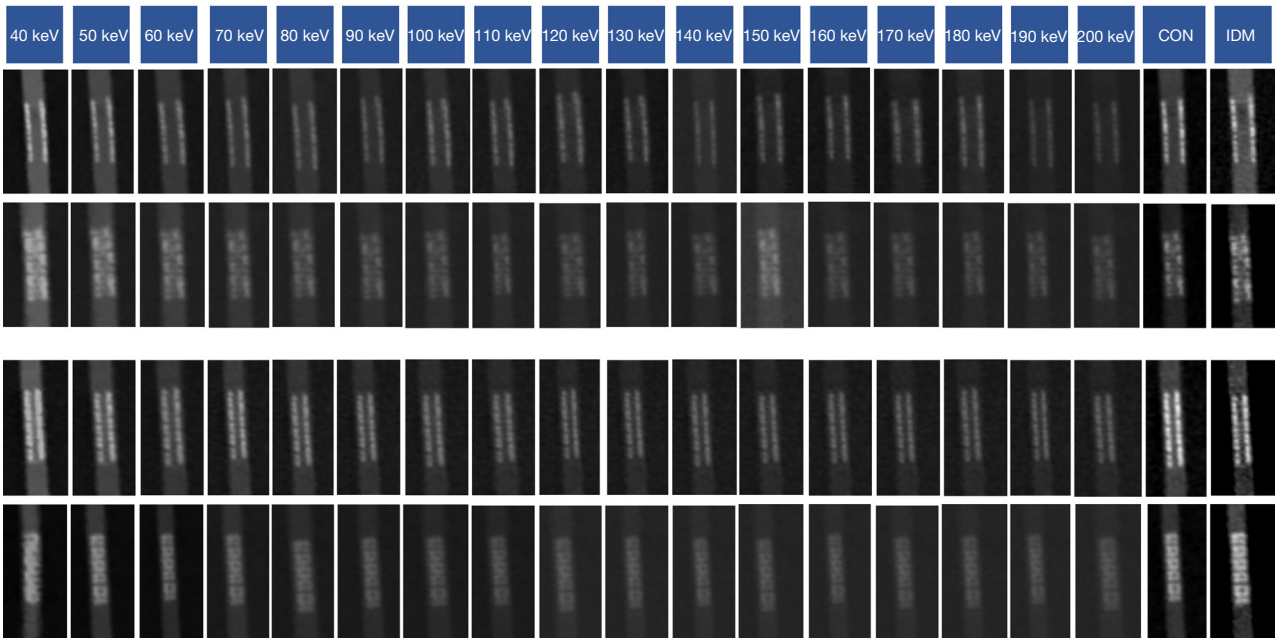

Figure 4 Monoenergetic images at 40–200 keV (a 10 keV interval), conventional images, and iodine density maps of a stent in group A (number 11, row 1–2) and group B (number 12, row 3–4). Group A was the group with stents <3 mm in diameter, and group B was the group with stents ≥3 mm in diameter. Row 1 and row 3 show the stent lumen, while row 2 and row 4 show the stent structure. CON, conventional images; IDM, iodine density maps.

monoenergetic images, conventional images, and iodine density maps were compared using the Friedman test and Dunn test. Additionally, quantitative parameters, including BAI, IDD, and SNR, were evaluated through repeated-measures analysis of variance (ANOVA) and the Tukey test.

Results

Subjective evaluation

The kappa values for stent lumen and structure were 0.83 (Z=21.3) and 0.89 (Z=22.6), respectively, indicating strong agreement between the two evaluating radiologists. The visualization quality of stent lumen and structure varied depending on the reconstruction types and energy level of monoenergetic imaging, as illustrated in *Figure 4*. The optimal energy level for monoenergetic imaging was determined to be 130 keV for group A and 90 keV for group B in terms of stent lumen. For both stent groups, the optimal monoenergetic images received the highest score. In group A, there were statistically significant differences in the stent lumen score between the optimal monoenergetic images (mean score of 2.56±0.51) and iodine density maps (mean score of 1.37±0.5), as depicted in *Figure 5A*. In group B, the stent lumen score of iodine density maps (mean score of 2.0±0.65) was significantly lower than that of optimal monoenergetic images (mean score of 3.1±0.55) and conventional images (mean score of 2.95±0.69), as shown in *Figure 5B*. Regarding stent structure, the optimal energy level for monoenergetic imaging was found to be 160 keV for group A and 90 keV for group B. For both stent groups, the iodine density maps received the highest score. For group A, the multiple comparisons revealed that the score of the conventional images (mean score of 1.88±1.03) was significantly lower than that of the optimal monoenergetic images (mean score of 2.75±1.0) and iodine density maps (mean score of 3.0±0.52), as shown in *Figure 5C*. For group B, the score of the conventional images (mean score of 3.0±0.73) was also significantly lower than that of iodine density maps (mean score of 3.8±0.41).

Quantitative evaluation

The results of the quantitative assessment are presented in *Table 2*. As the energy level of the monoenergetic images increased from 40 to 200 keV, the SNR_{is} for group A and

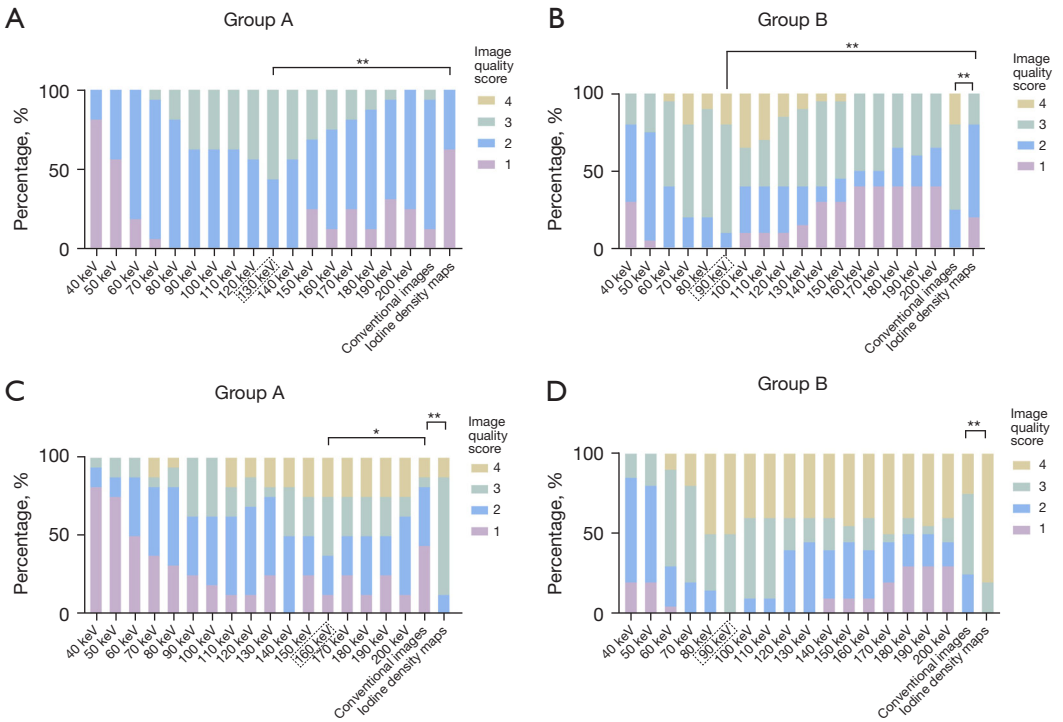

Figure 5 Subjective assessment score of stent lumen and structure. (A) Subjective score of stent lumen for group A. (B) Subjective score of stent lumen for group B. (C) Subjective score of stent structure for group A. (D) Subjective score of stent structure for group B. Group A was the group with stents <3 mm in diameter, and group B was the group with stents ≥3 mm in diameter. The dashed boxes indicate the energy level of optimal monoenergetic imaging. *, P<0.05; **, P<0.01.

group B decreased steadily from 41.26±30.63 and 21.5±8.83 to 14.53±10.7 and 7.31±5.2, respectively. The SNR_{ns} exhibited a similar tendency, decreasing from 77.5±32.76 and 57±14.4 to 8.55±2.94 and 5.51±1.65, for group A and group B, respectively. For group A, multiple comparisons showed that there was no significant difference in the SNR_{is} among the optimal monoenergetic (40 keV), conventional images, or iodine density maps. For group B, the SNR_{is} for the optimal monoenergetic (40 keV) was significantly greater than that of iodine density maps. For both stent groups, the SNR_{ns} of the optimal monoenergetic (40 keV) was also significantly higher than that of the conventional images and iodine density maps. The mean SNR_{is} and SNR_{ns} of each image set for both stent groups are shown in *Figure 6A* and *Figure 6B*, respectively.

In terms of IDD, the optimal energy level was 110 keV for group A and 150 keV for group B. For both stent groups, the iodine density maps provided the lowest IDD value. For group A, multiple comparison showed significant differences between the optimal monoenergetic images and conventional images. For group B, no significant difference was observed between the optimal monoenergetic images, conventional images, and iodine density maps. As for BAI, the optimal energy level was 110 keV for group A and 130 keV for group B. Similarly, for both stent groups, the iodine density maps provided the lowest BAI value. For group A, multiple comparison showed significant differences between the optimal monoenergetic images and conventional images. For group B, no significant difference was observed between the optimal monoenergetic images, conventional images, and iodine density maps. The mean IDD and BAI of each image set for both stent groups are shown in *Figure 6C* and *Figure 6D*, respectively.

Discussion

This study evaluated the effectiveness of monoenergetic images and iodine density maps in visualizing the stent lumen and structure on the dual-layer detector spectral CT compared to conventional CT images. The wider detector

Table 2 Mean measured quantitative parameters and P value for analysis of variance

Image set	SNR_{is}		SNR_{ns}		IDD (%)		BAI (%)	
	<3 mm	≥3 mm	<3 mm	≥3 mm	<3 mm	≥3 mm	<3 mm	≥3 mm
40 keV	41.26±30.63[#]	21.5±8.83[#†]	77.5±32.76[#†‡]	57±14.4[#†‡]	79.75±7.52	32.77±22.75	86.66±5.2	67.47±8.07
50 keV	37.04±28.71	20.7±7.87	52.11±17.88	40.2±8.49	74.21±11.4	24.75±17.84	82.62±7.86	62.61±5.75
60 keV	30.23±23.57	20.6±7.58	37.14±12.64	28.4±6.96	72.9±6.94	27.34±21.63	81.81±4.69	63.71±7.99
70 keV	31.13±16.22	16.9±5.86	27.97±9.809	21.4±5.56	71.16±5.9	19.6±21.66	80.78±4.06	59.51±6.49
80 keV	25.82±14.64	14.7±5.11	22.04±7.711	17±4	70.04±7.81	24.2±22.25	79.6±5.24	61.69±7.84
90 keV	19.98±12.64	12.3±5.93	18.3±6.202	13.9±3.27	67.4±8.7	13.95±25.27	77.76±6.07	55.93±8.39
100 keV	21.68±9.56	12±4.19	15.77±5.215	11.3±3.37	68.67±7.78	16.68±28.35	78.73±4.85	57.63±11
110 keV	19.96±9.43	10.9±4.24	13.93±4.77	10±2.58	65.74±6.7[#†]	13.29±26.15	76.87±4.01[#‡]	55.5±10.3
120 keV	18.64±9.45	10.5±4.17	12.55±4.403	8.87±2.38	66.99±6.69	14.93±27.53	77.34±3.6	56.52±10.8
130 keV	17.6±9.63	9.51±4.77	11.41±3.92	8.04±2.18	67.19±7.09	14.45±28.8	77.22±4.21	54.59±13.1[#]
140 keV	16.76±9.89	9.45±4.3	10.87±3.76	7.44±2.06	67.67±9.93	14.88±27.27	77.67±6.59	56.27±10.1
150 keV	16.21±10.02	8.83±4.52	10.14±3.471	6.87±1.95	67.4±10.3	11.96±27.24[#]	77.58±6.81	55.14±9.81
160 keV	15.77±10.23	8.82±4.46	9.53±3.44	6.47±1.87	67.86±8.73	14.04±26.68	77.69±5.25	56.57±9.41
170 keV	15.36±10.38	8.59±4.5	9.184±3.22	6.11±1.79	66.78±9.27	14.95±25.6	76.97±5.65	57.53±8.91
180 keV	14.76±10.91	7.98±4.91	8.97±3.132	5.89±1.74	76.39±23.5	15.28±27.27	83.36±15.5	57.48±9.38
190 keV	14.76±10.65	8.22±4.55	8.74±3.06	5.69±1.69	69.89±6.43	13.95±29.05	79.73±4.16	56.84±10.5
200 keV	14.53±10.7	7.31±5.2	8.55±2.94	5.51±1.65	71.16±6.55	15.48±30.2	80.49±4	57.65±10.9
Conventional images	30.57±13.05	16.4±4.14	28.89±10.1[†]	21.4±3.5[†]	59.93±10.3[†]	12.96±22.16	72.13±6.44[‡]	56.05±7.34
Iodine density maps	24.74±13.54	12.9±5.22[†]	24.72±8.81[‡]	19.3±4.8[‡]	59.72±9.55	5.81±23.35	71.62±6.57	49.7±10.1
F value	3.69	14.35	30.52	79.41	4.38	0.828	5.63	2.03
P	0.079	<0.001	<0.001	<0.001	0.044	0.408	0.028	0.171

Data are presented as mean ± standard deviation. [#], the optimal energy level for monoenergetic imaging; [†] and [‡] indicate the pairs with P<0.05 in multiple comparisons. SNR_{is}, in-stent lumen signal-to-noise ratio; SNR_{ns}, non-stent lumen signal-to-noise ratio; IDD, internal diameter difference; BAI, blooming artifact index.

(8 cm) of the second-generation dual-layer detector CT improves the temporal resolution of coronary CT angiography on spectral imaging. However, the widening of the detector may complicate the transmission path of X-rays and make it more difficult to correct the interlayer scattering effect, potentially leading to a deterioration in image quality (21). Although some studies have explored the expanded applications of stent lumen imaging on dual-layer detector CT, there is still a lack of research on the quality of stent lumen and structure imaging specifically on second-generation dual-layer detector CT (22,23). Therefore, we conducted an updated *in vitro* study to provide new insights into the in-stent lumen imaging capacity of the second-generation dual-layer CT.

Previous studies using the first-generation dual-layer CT have shown that monoenergetic imaging is effective in delineating in-stent lumens. This is attributed to the ability of material decomposition in the raw-data domain. Liu *et al.* reported that the optimal energy level for monoenergetic stent lumen imaging was 80 keV, while Zhang *et al.* indicated that 90 keV provided the best image quality (8,23). In our study, we found that 130 and 90 keV were the optimal energy levels for group A and group B, respectively. These findings suggest that monoenergetic imaging should be tailored to stent diameters in clinical practice. For smaller diameter stents, higher energy X-ray photons are

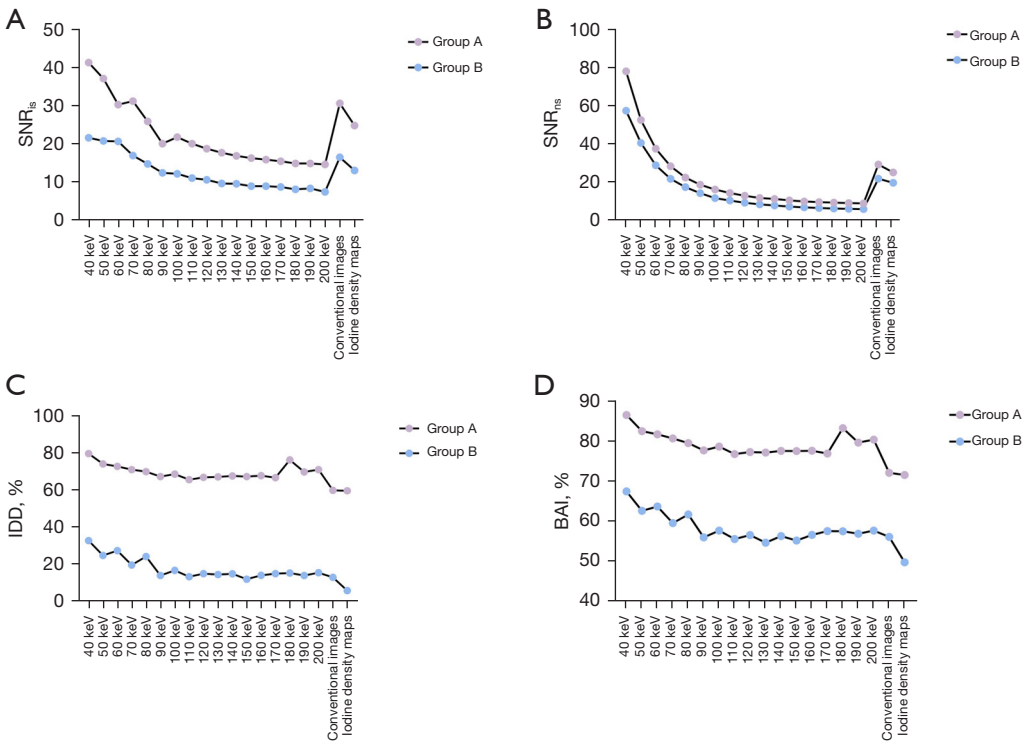

Figure 6 The mean SNR_{is}, SNR_{ns}, IDD, and BAI of each image set for both stent groups. Group A was the group with stents <3 mm in diameter, and group B was the group with stents ≥3 mm in diameter. Note that the curves of SNR_{ns} are smoother than those of SNR_{is}. SNR_{is}, in-stent lumen signal-to-noise ratio; SNR_{ns}, non-stent lumen signal-to-noise ratio; IDD, internal diameter difference; BAI, blooming artifact index.

required to enhance penetration ability and mitigate beam hardening effects on lumen visualization. The inconsistency with the optimal energy level found in previous studies could be due to differences in stent materials and diameters. In terms of stent structure imaging, our study revealed that the iodine density maps were superior to both the optimal monoenergetic images and conventional images, regardless of stent diameter. According to Symons *et al.*, iodine density cannot differentiate between in-stent and non-stent coronary arteries (24). Therefore, the application of the iodine density maps effectively reduces the influence of beam hardening artifacts on the visibility of stent trabeculae, improving the visualization of stent structure and the detection of stent-related restenosis, such as mal-expansion, fracture, and retraction in clinical practice.

SNR is an important objective index for image evaluation. In our study, the energy level of the monoenergetic imaging increased, and the SNR for both the in-stent lumen and non-stent lumen decreased, which is consistent with previous studies (8,24,25). The specific anticorrelation denoising algorithm used in the dual-layer detector CT may contribute to achieving uniformly low noise across different energy levels in monoenergetic imaging (26). SNR is influenced by the attenuation of the ROI and the background noise. Since the background noise is consistently low, a decrease in energy level would result in a positive correlation with SNR. Furthermore, our study found that the SNR of the optimal monoenergetic images was significantly higher than that of conventional images and iodine density maps. This suggests that monoenergetic imaging could be a preferable option for improving SNR in clinical practice. However, increased SNR does not necessarily mean improved image quality, as an *in-vivo* study showed (27). The subjective image quality should be also considered when pursuing the increase of SNR. We noted that there were large intragroup variations in the SNR, which were induced by the intragroup differences in stent diameter and material.

IDD refers to the difference between the internal diameter measured by CT and the actual internal

diameter determined by IVUS. Previous studies have only focused on the CT-measured and nominal diameters for IDD evaluation (17). However, the actual diameters may differ from the nominal diameters. Improper stent placement, both underexpansion or overexpansion can cause deviation between the actual and nominal diameters, potentially impacting the accuracy of IDD evaluation. To address this, we used IVUS, which provides highly accurate measurements of the internal stent diameter (28), immediately after CT scanning to avoid any discrepancies between the actual and nominal diameter that could affect IDD accuracy. A previous study reported that the mean IDD in conventional images range from 41% to 63%, and another study reported a mean IDD of 50.7%. In our study, the range of mean IDDs of group A (from 59.72% to 79.75%) was higher than that reported previously, and the mean IDDs of group B (from 5.81% to 32.77%) were lower. However, previous research included nominal diameters for IDD evaluation, and we used IVUS to measure the actual internal diameter. Moreover, 32.1% (18/56) and 43.8% (7/16) of stents in the two studies mentioned above were made from 316 L stainless stee, which we did not examine. Differences in methodology and stent material inevitably result in differences in the absolute IDD values. Thus, it is more important to compare the variation trend than to compare the absolute values. Previous studies have shown that the visible internal diameter gradually increases with higher energy levels of monoenergetic imaging (22,29). In our study, both stent groups exhibited slight fluctuations in IDD, suggesting that monoenergetic imaging may have limited additional value in improving the accuracy of internal diameter measurement. There were no significant differences between the iodine density maps, optimal monoenergetic images, and conventional images. However, the iodine density maps yielded the lowest IDD, possibly due to the enhanced material decomposition ability of the dual-layer detector CT. Considering that iodine density mapping can be automatically generated and is superior to IDD, we expect it can improve the in-stent restenosis assessment when combined with CCTA and other state-of-the-art technologies, such as deep learning image reconstruction (30).

It has been observed that the blooming artifacts in monoenergetic images gradually decrease with increasing energy level (31). Our study also demonstrated that the BAI decreased as the energy level increased from 40 to 90 keV and then stabilized at 100 keV. There were no significant differences between the iodine density maps, optimal monoenergetic images, and conventional images. However, the iodine density maps appeared to be superior in terms of providing the lowest BAI. In addition, iodine density maps can be automatically generated during postprocessing without any manual input, while the optimal monoenergetic imaging requires manual input of various energy levels for identifying the optimal energy level. This suggests that the iodine density maps may be a more efficient and accurate option for geometric measurement in clinical practice. We noted that there were large intragroup variations in the BAI and IDD value, which were induced by the differences in the severity of metal artifacts and intrinsically caused by the intragroup differences in stent diameter and material.

This study involved certain limitations that should be acknowledged. First, the stent number was limited (only three vendors). Second, the monoenergetic images were reconstructed at a 10-keV interval in order to reduce the postprocessing burden. However, the actual optimal energy level may fall within the reconstruction interval, and was not evaluated. Despite this limitation, the study did evaluate the effect of energy level on subjective and quantitative assessment. Third, the static stents were oriented parallel to the Z-axis of the CT, which differs from the moving and often orientation-changing implanted stents in real clinical practice. Fourth, this study was conducted without a flow condition, and thus there may be other relevant factors to consider in applying the study results to clinical practice. However, it is likely that both monoenergetic images and iodine density maps will improve the visualization of lumen and structure, as well as the accuracy of geometry measurement. Based on the results of the current phantom study, we will conduct further *in vivo* study on in-stent restenosis assessment using digital subtraction angiography and/or IVUS as reference standard to further validate the clinical usefulness of the iodine density maps and monoenergetic images.

Conclusions

The use of monoenergetic images and iodine density maps on the dual-layer detector CT provides several advantages. Monoenergetic images are beneficial for lumen visualization, while iodine density maps are useful for stent structure assessment. In terms of geometry assessment, the iodine density maps outperformed both the optimal monoenergetic images and conventional images. In clinical practice, it is necessary to comprehensively consider which image to use based on the given task.

Acknowledgments

Funding: This study was supported by the Institutional Foundation of The First Affiliated Hospital of Xi'an Jiaotong University (No. 2021ZYTS-01), and the Foundation of Key Research and Development Plan of Shaanxi Province of China (No. 2023-YBSF-403).

Footnote

Conflicts of Interest: All authors have completed the ICMJE uniform disclosure form (available at https://qims.amegroups.com/article/view/10.21037/qims-24-786/coif). N.P. reports being a full-time employee of Bayer Healthcare Company during the conduct of the study. S.D. and Y.Z. report being full-time employees of Philips Healthcare during the conduct of the study. The other authors have no conflicts of interest to declare.

Ethical Statement: The authors are accountable for all aspects of the work in ensuring that questions related to the accuracy or integrity of any part of the work are appropriately investigated and resolved.

References

1. Martin SS, Aday AW, Almarzooq ZI, Anderson CAM, Arora P, Avery CL, et al. 2024 Heart Disease and Stroke Statistics: A Report of US and Global Data From the American Heart Association. Circulation 2024;149:e347-913.
2. Park SJ, Ahn JM, Kang DY, Yun SC, Ahn YK, Kim WJ, et al. Preventive percutaneous coronary intervention versus optimal medical therapy alone for the treatment of vulnerable atherosclerotic coronary plaques (PREVENT): a multicentre, open-label, randomised controlled trial. Lancet 2024;403:1753-65.
3. Giustino G, Colombo A, Camaj A, Yasumura K, Mehran R, Stone GW, Kini A, Sharma SK. Coronary In-Stent Restenosis: JACC State-of-the-Art Review. J Am Coll Cardiol 2022;80:348-72.
4. Weiss AJ, Lorente-Ros M, Correa A, Barman N, Tamis-Holland JE. Recent Advances in Stent Technology: Do They Reduce Cardiovascular Events? Curr Atheroscler Rep 2022;24:731-44.
5. Marano R, Rovere G, Savino G, Flammia FC, Carafa MRP, Steri L, Merlino B, Natale L. CCTA in the diagnosis of coronary artery disease. Radiol Med 2020;125:1102-13.
6. Hamon M, Champ-Rigot L, Morello R, Riddell JW, Hamon M. Diagnostic accuracy of in-stent coronary restenosis detection with multislice spiral computed tomography: a meta-analysis. Eur Radiol 2008;18:217-25.
7. Eckert J, Renczes-Janetzko P, Schmidt M, Magedanz A, Voigtländer T, Schmermund A. Coronary CT angiography (CCTA) using third-generation dual-source CT for ruling out in-stent restenosis. Clin Res Cardiol 2019;108:402-10.
8. Liu Q, Wang Y, Qi H, Yu Y, Xing Y. Exploring the best monochromatic energy level in dual energy spectral imaging for coronary stents after percutaneous coronary intervention. Sci Rep 2021;11:17576.
9. Tian X, Chen Y, Pan S, Lan H, Cheng L. Enhanced in-stent luminal visualization and restenosis diagnosis in coronary computed tomography angiography via coronary stent decomposition algorithm from dual-energy image. Comput Biol Med 2024;171:108128.
10. Hickethier T, Wenning J, Bratke G, Maintz D, Michels G, Bunck AC. Evaluation of soft-plaque stenoses in coronary artery stents using conventional and monoenergetic images: first in-vitro experience and comparison of two different dual-energy techniques. Quant Imaging Med Surg 2020;10:612-23.
11. Agostini A, Borgheresi A, Mari A, Floridi C, Bruno F, Carotti M, Schicchi N, Barile A, Maggi S, Giovagnoni A. Dual-energy CT: theoretical principles and clinical applications. Radiol Med 2019;124:1281-95.
12. Ding Q, Niu T, Zhang X, Long Y. Image-domain multimaterial decomposition for dual-energy CT based on prior information of material images. Med Phys 2018. [Epub ahead of print]. doi: 10.1002/mp.13001.
13. Aslan S, Camlidag I, Nural MS. Lower energy levels and iodine-based material decomposition images increase pancreatic ductal adenocarcinoma conspicuity on rapid kV-switching dual-energy CT. Abdom Radiol (NY) 2019;44:568-75.

14. Zopfs D, Lennartz S, Große Hokamp N, Rau K, Zaeske C, Laukamp KR, Houbois C, Luers JC, Maintz D, Puesken M. Head and neck squamous cell carcinoma: evaluation of iodine overlay maps and low-energy virtual monoenergetic images acquired with spectral detector CT. Clin Radiol 2022;77:e425-33.
15. Große Hokamp N, Maintz D, Shapira N, Chang H, Noël PB. Technical background of a novel detector-based approach to dual-energy computed tomography. Diagn Interv Radiol 2020;26:68-71.
16. Rassouli N, Etesami M, Dhanantwari A, Rajiah P. Detector-based spectral CT with a novel dual-layer technology: principles and applications. Insights Imaging 2017;8:589-98.
17. André F, Korosoglou G, Hosch W, Giannitsis E, Kauczor HU, Katus HA, Steen H. Performance of dual source versus 256-slice multi-slice CT in the evaluation of 16 coronary artery stents. Eur J Radiol 2013;82:601-7.
18. Taylor AJ, Cerqueira M, Hodgson JM, Mark D, Min J, O'Gara P, Rubin GD; . ACCF/SCCT/ACR/AHA/ASE/ASNC/NASCI/SCAI/SCMR 2010 Appropriate Use Criteria for Cardiac Computed Tomography. A Report of the American College of Cardiology Foundation Appropriate Use Criteria Task Force, the Society of Cardiovascular Computed Tomography, the American College of Radiology, the American Heart Association, the American Society of Echocardiography, the American Society of Nuclear Cardiology, the North American Society for Cardiovascular Imaging, the Society for Cardiovascular Angiography and Interventions, and the Society for Cardiovascular Magnetic Resonance. J Cardiovasc Comput Tomogr 2010;4:407.e1-33.
19. Funama Y, Oda S, Utsunomiya D, Taguchi K, Shimonobo T, Yamashita Y, Awai K. Coronary artery stent evaluation by combining iterative reconstruction and high-resolution kernel at coronary CT angiography. Acad Radiol 2012;19:1324-31.
20. Boccalini S, Si-Mohamed SA, Lacombe H, Diaw A, Varasteh M, Rodesch PA, Villien M, Sigovan M, Dessouky R, Coulon P, Yagil Y, Lahoud E, Erhard K, Rioufol G, Finet G, Bonnefoy-Cudraz E, Bergerot C, Boussel L, Douek PC. First In-Human Results of Computed Tomography Angiography for Coronary Stent Assessment With a Spectral Photon Counting Computed Tomography. Invest Radiol 2022;57:212-21.
21. Taguchi K, Iwanczyk JS. Vision 20/20: Single photon counting x-ray detectors in medical imaging. Med Phys 2013;40:100901.
22. Qin L, Gu S, Chen C, Zhang H, Zhu Z, Chen X, Han Q, Yan F, Yang W. Initial exploration of coronary stent image subtraction using dual-layer spectral CT. Eur Radiol 2019;29:4239-48.
23. Zhang D, Xie Y, Wang Y, Guo N, Wang Y, Jin Z, Xue H. Initial Clinical Experience of Virtual Monoenergetic Imaging Improves Stent Visualization in Lower Extremity Run-Off CT Angiography by Dual-Layer Spectral Detector CT. Acad Radiol 2020;27:825-32.
24. Symons R, De Bruecker Y, Roosen J, Van Camp L, Cork TE, Kappler S, Ulzheimer S, Sandfort V, Bluemke DA, Pourmorteza A. Quarter-millimeter spectral coronary stent imaging with photon-counting CT: Initial experience. J Cardiovasc Comput Tomogr 2018;12:509-15.
25. Huang X, Gao S, Ma Y, Lu X, Jia Z, Hou Y. The optimal monoenergetic spectral image level of coronary computed tomography (CT) angiography on a dual-layer spectral detector CT with half-dose contrast media. Quant Imaging Med Surg 2020;10:592-603.
26. Ehn S, Sellerer T, Muenzel D, Fingerle AA, Kopp F, Duda M, Mei K, Renger B, Herzen J, Dangelmaier J, Schwaiger BJ, Sauter A, Riederer I, Renz M, Braren R, Rummeny EJ, Pfeiffer F, Noël PB. Assessment of quantification accuracy and image quality of a full-body dual-layer spectral CT system. J Appl Clin Med Phys 2018;19:204-17.
27. Kazimierczak W, Nowak E, Kazimierczak N, Jankowski T, Jankowska A, Serafin Z. The value of metal artifact reduction and iterative algorithms in dual energy CT angiography in patients after complex endovascular aortic aneurysm repair. Heliyon 2023;9:e20700.
28. Whiteside HL, Nagabandi A, Kapoor D. Stentablation with Rotational Atherectomy for the Management of Underexpanded and Undilatable Coronary Stents. Cardiovasc Revasc Med 2019;20:1203-8.
29. Hickethier T, Baeßler B, Kroeger JR, Doerner J, Pahn G, Maintz D, Michels G, Bunck AC. Monoenergetic reconstructions for imaging of coronary artery stents using spectral detector CT: In-vitro experience and comparison to conventional images. J Cardiovasc Comput Tomogr 2017;11:33-9.
30. Wang Y, Wang G, Huang X, Zhao W, Zeng Q, Li Y, Guo J. Improving image quality and resolution of coronary arteries in coronary computed tomography angiography by using high-definition scans and deep learning image reconstruction. Quant Imaging Med

Surg 2023;13:2933-40.
31. Van Hedent S, Große Hokamp N, Kessner R, Gilkeson R, Ros PR, Gupta A. Effect of Virtual Monoenergetic Images From Spectral Detector Computed Tomography on Coronary Calcium Blooming. J Comput Assist Tomogr 2018;42:912-8.

Cite this article as: Chen L, Pan N, Hu B, Li Y, Dong S, Zhou Y, Guo J, Yang J, Luo Y, Jian Z. Monoenergetic reconstructions and iodine density maps for visualization of coronary artery stents using 8-cm dual-layer detector spectral computed tomography: an *in vitro* phantom study. Quant Imaging Med Surg 2024;14(10):7671-7683. doi: 10.21037/qims-24-786